Supporting Information: Beam steering with a nonlinear optical phased array antenna

Sebastian Busschaert,[1] Nikolaus Flöry,[1] Sotirios Papadopoulos,[1]
Markus Parzefall,[1] Sebastian Heeg,[1] and Lukas Novotny[1,*]
[1] *Photonics Laboratory, ETH Zürich, Zürich, Switzerland*

I. NONLINEAR SETUP

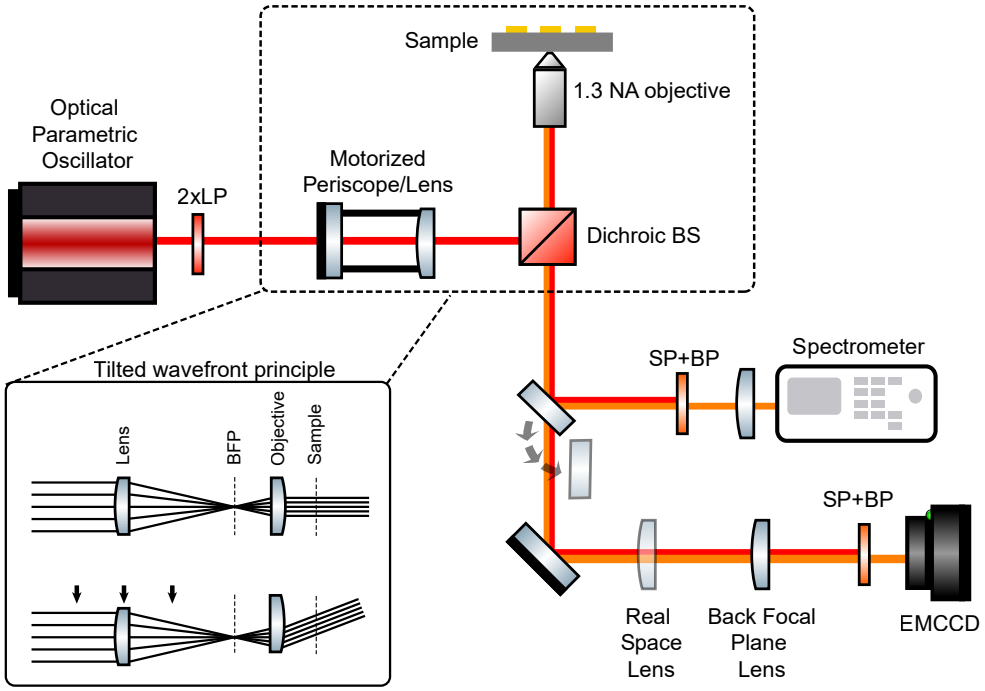

Fig. S 1. Illustration of setup for nonlinear measurements. The beam path starts at the optical parametric oscillator (Coherent Mira-OPO) that produces 200 fs pulses with a repitition rate of 76 MHz. The laser is subsequently spectrally filtered with the following components: Semrock BL 1110LP, Chroma HHQ940LP. Afterwards the beam enters a periscope (mirrors mounted at 90° angle) that is motorized using two translation stages (PT1/M-Z8, Thorlabs) and connected to a lens (AC254-400-C-ML, Thorlabs). The beam gets reflected at a dichroic beamsplitter (DMSP950R by Thorlabs) and enters an oil immersion objective (1.3 NA Plan Fluor 100x Nikon) after which it hits the sample and produces the nonlinear signal. The signal passes the dichroic beamsplitter and can either be send to a spectrometer (Acton SP2300 with Pixis100 CCD) or to an EMCCD (Acton Photon Max 512) by using a flip mirror. The EMCCD is able to image either the real space of the sample or the back focal plane of the objective by choosing an appropriate lens before. Before the detectors, additional filters (770SP, 650/60BP for SHG, 561SP for THG, all filters by Semrock) only pass the wanted nonlinear signal. Abbreviations: LP - longpass filter, SP - shortpass filter, BP - bandpass filter, BS - beamsplitter, BFP - back focal plane.

For the nonlinear measurements the attached lens mounted to the motorized periscope enabled us to focus the laser onto the back focal plane (BFP) of the oil immersion objective and thus created a collimated illumination at the sample stage. Since the resulting beamspot in the sample plane ($\approx$ 10–15 µm) is larger than the array size ($\approx$ 8 µm), the illumination leads to an excitation of the nanorods with zero phase delay. Any lateral displacement of the focused beam from the optical axis leads to a tilt in the exciting wavefront (illustrated in Figure S1). The tilted wavefront leads to a linear phase gradient in the excitation of the nanorods, thus constituting a non-zero phase delay. It was paramount to both move the beam and the lens simultaneously (by attaching the lens to the periscope) in order to ensure non-distorted tilting of the wavefront. Only moving the lens or tilting the beam before the lens would have

* lnovotny@ethz.ch

resulted in an axial displacement and hence an uneven illumination of the whole array.

In order to write ETH a script for the motorized stages was implemented using the Kinesis software from Thorlabs. The script consisted of sequential movements perpendicular to the optical axis, that were captured by the EMCCD using a longer integration time (50 seconds).

II. CHARACTERIZATION

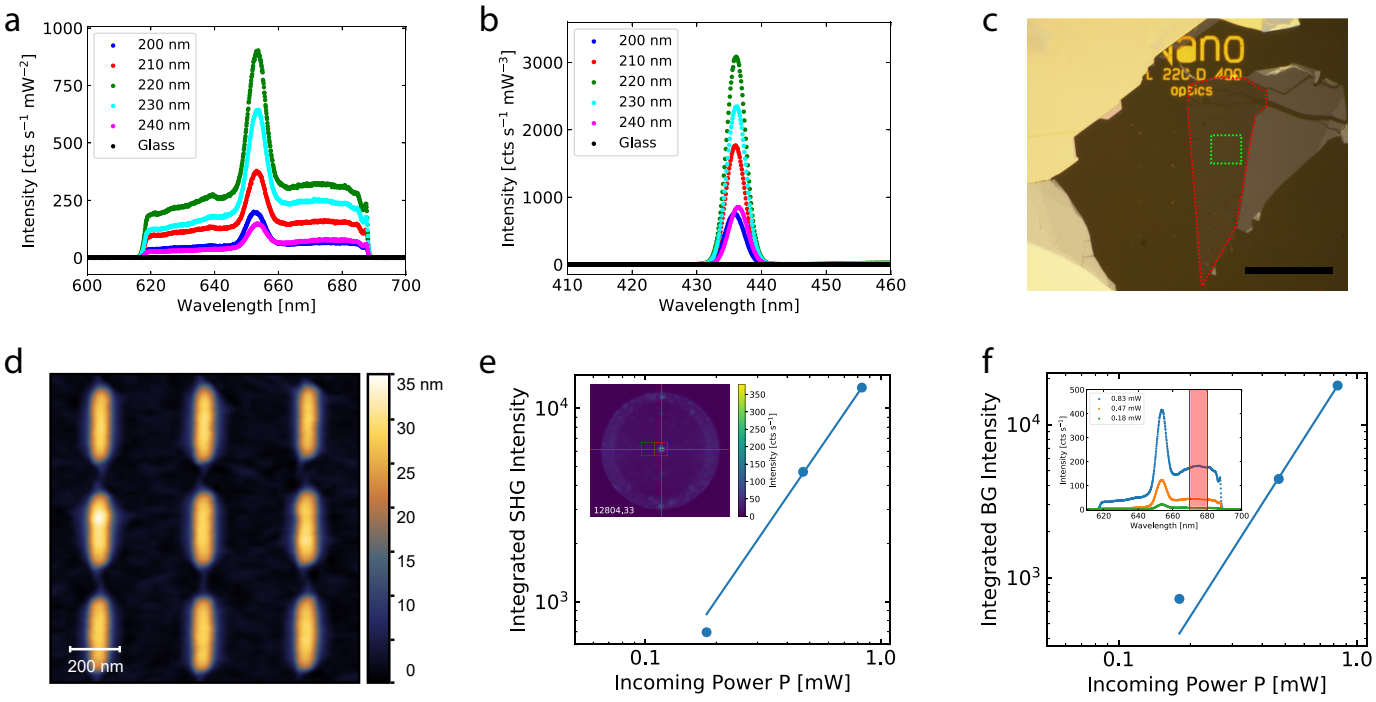

Fig. S 2. Characterization of bare gold arrays and final MoS_2-array device. (a,b) SHG, THG responses of arrays for various rod lengths. The 220 nm rods scatter the strongest. (c) Bright field image of final device. The monolayer MoS_2 is indicated with a red dashed line, the array with a green dashed line. The scale-bar is 25 µm. (d) AFM scan of the coupled system, demonstrating the folding of the MoS_2 over the rods. (e) Power-dependent integrated SHG intensities of the coupled MoS_2-array system. The data was evaluated by summing over a certain pixel area in the recorded BFP images (see inset, the green box indicates the background data that was subtracted). The line indicates a fit corresponding to $I(P) = A \times P^{1.8\pm0.1}$, thus agreeing with the expected nonlinear order. (f) Power-dependent integrated background (BG) intensities of the coupled MoS_2-array system. The data was evaluated by integrating the respective spectra, see inset (red box indicates the integration boundaries). The line corresponds to a fit with a functional form of $I(P) = A \times P^{2.4\pm0.1}$, which indicates a mix of multiphoton processes.

III. POLAR PLOT REPRESENTATION

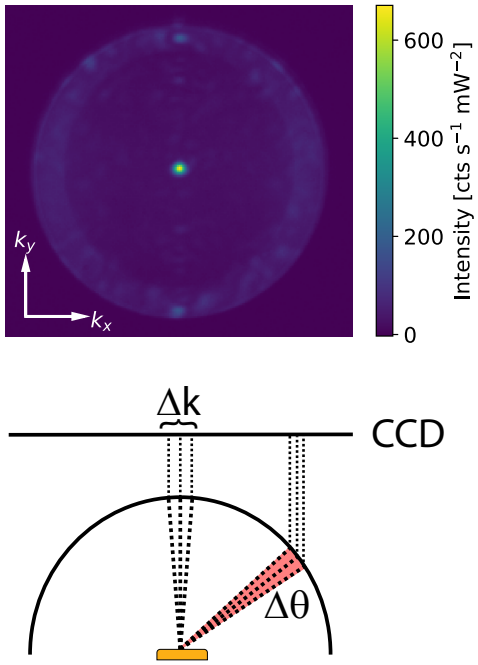

Fig. S 3. Angular projection of the emission on the CCD plane. Depending on the radiation angle with respect to the rod, the same angular spread $\Delta\phi$ can lead to a different Δk.

Imaging the back focal plane of the 1.3 NA oil immersion objective onto a CCD leads to a projection of the k-space, which can be transformed into an emission angle ϕ-dependent polar plot representation. The recorded image is linear in pixels, i.e. $k_{x,y}$, and gives us an emission intensity with the unit counts per Δk - the transformation into an emission with unit counts per $\Delta\phi$ requires the casting of $\frac{1}{\Delta k}$ into $\frac{1}{\Delta\phi}$. This is not a linear transformation as illustrated in Figure S3. Since we project onto a circle (i.e. collection lens), Δk is bigger for small emission angles and decreases for larger emission angles. This leads to higher recorded intensity per pixel since the emission is captured by less pixels. In order to account for that, we used the inner ring in the recorded images (dashed line) as a normalization, since

$$\phi_{NA=1} = \arcsin \frac{n_{air}}{n_{glass}} = 41.14° \tag{1}$$

With that we could assign an angle $\phi_{NA=1}$ to certain pixel values, construct an array of $k_{x,y}$ values in between ($k_{x,y} \sim px$) and then calculate the corresponding angle values using

$$\phi = \arcsin \frac{k_{x,y}}{k} \tag{2}$$

The wavevector k is given by $k = \frac{2\pi}{\lambda_{SHG}}$. By then calculating $\Delta\phi = \phi_{i+1} - \phi_i$ we arrive at the desired transformation with unit deg^{-1}. Additionally, the pixels of the detector also have a finite size orthogonal to the evaluated emission direction. By multiplying with the angle-transformed pixel width at the center of the CCD an expression with the unit deg^{-2} is generated. To comply with SI unit standards we transform deg^{-2} into µsr^{-1}.

IV. ANTENNA EMISSION PATTERN

For the angle dependency of the emission we used the analytical far field solution of two opposite dipoles:

$$I_{\mathrm{quad,em}} = 4\left|\cos\phi \sin\frac{\pi d \sin\phi}{\lambda}\right|^2 \tag{3}$$

Here d is the separation between the dipoles and is given by the rod length $d = 220\,\mathrm{nm}$. The wavelength was chosen to be $\lambda = \frac{655\,\mathrm{nm}}{1.52}$ since the system sits on glass ($n_{\mathrm{glass}} = 1.52$) and we observe the emission through an oil immersion objective with the same refractive index.
The excitation is described by a term that describes the angle-dependent plasmon resonance

$$I_{\mathrm{exc}} = (\cos^2\phi)^2 \tag{4}$$

The term is to the power of 2 due to the nonlinear order of SHG.
The second term for the excitation is due to a change of the intensity when changing the incoming wavefront. This effect is the inverse problem to the angular representation discussed in Figure S3. The focus in the back focal plane of the objective remains constant in size, but with larger displacement from the center (and larger angular spread) the light is sent onto a smaller area in the sample plane. The incoming power remains constant throughout - hence, for larger angles the intensity increases according to:

$$I_{\mathrm{trans}} = \frac{1}{\cos^2\phi} \tag{5}$$

For the expression for the MoS_2-array system we added a term that describes the dipolar emission characteristic of the TMDC. Since the term for the opposite dipoles and the dipolar term can interfere with each other, we added the respective electric fields and then squared the expression

$$|E_{\mathrm{quad,em}} + E_{\mathrm{dipole,em}}|^2 = \left|\cos\phi\left(1 - 2i\sin\frac{\pi d\sin\phi}{\lambda}\right)\right|^2 \tag{6}$$

Both final expressions were then fitted to the data, the bare array with one fitting parameter, the MoS_2-array system with two parameters.

V. ENHANCEMENT

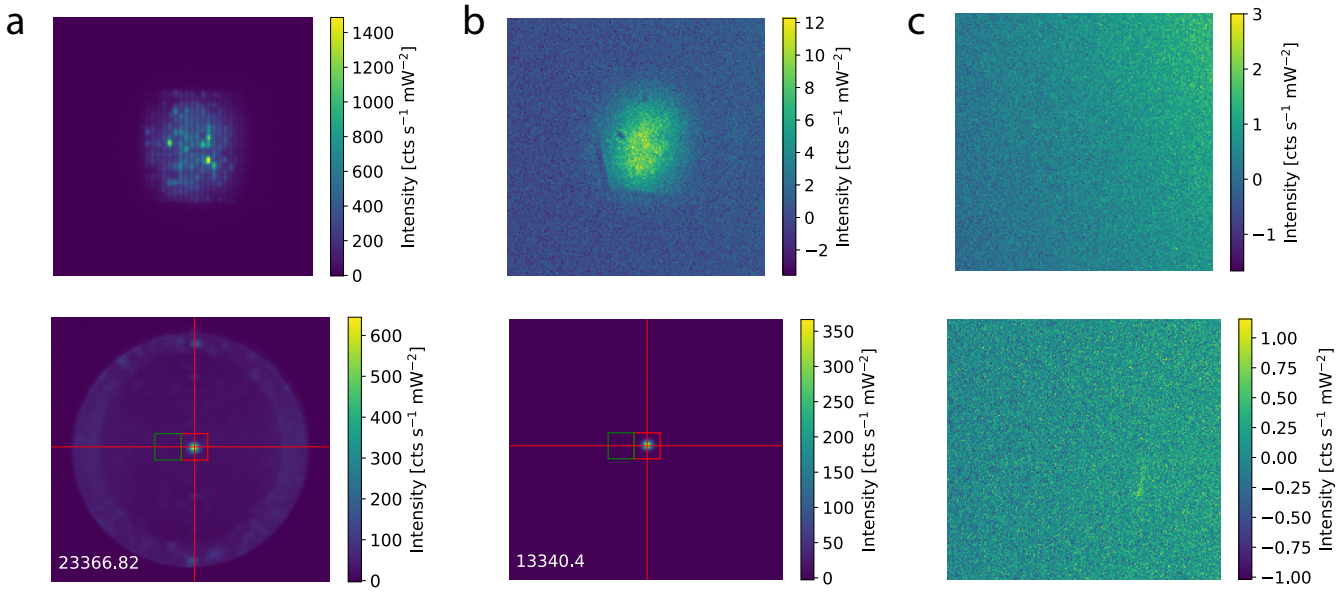

Fig. S 4. SHG enhancement of MoS_2-array system. Measured SHG real space and back focal plane (BFP) images of (a) MoS_2-array system, (b) bare MoS_2 and (c) glass. The emission feature in the center of the BFP images is integrated, the red box indicates the area (20x20 pixels) of the integrated signal S and the green box the integrated area for background subtraction S_{bg}. The white number indicates the total nonlinear signal $I = S - S_{bg}$. This measurement was repeated three times with slightly varying beam spot placement, resulting in a calculated SHG enhancement of $\frac{I_{system}}{I_{MoS_2}} \approx 1.6$.

VI. NON-RESONANT EXCITATION

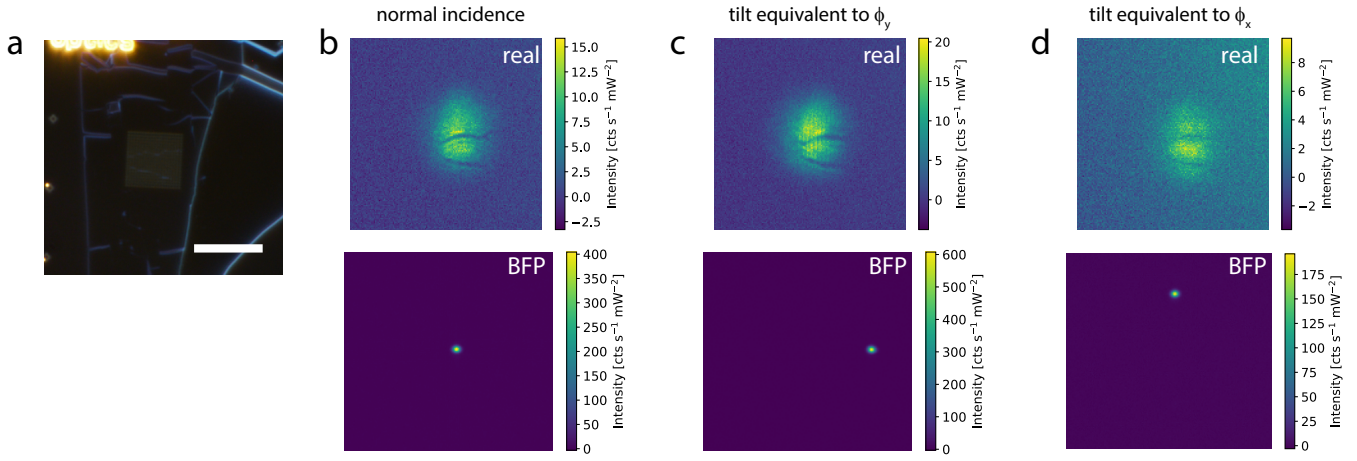

Fig. S 5. SHG measurements of MoS_2-array system with the incident polarization non-resonant with the rods (sample was rotated by 90°) (a) Dark field microscope image of measured system. Two cracks in the MoS_2 above the array are visible, giving a distinct feature for orientation. Scale bar: 10 μm (b) Real space and back focal plane (BFP) images of SHG under normal incidence. The cracks observed in (a) are seen in the real space image. (c,d) Real space and BFP images under tilt which is equivalent to a tilt in ϕ_y,ϕ_x direction as assigned in the main text. In contrast to the resonant excitation (described in the main text), no grating orders are observed under tilt for non-resonant excitation.

VII. NOISE STUDY OF K-SPACE MEASUREMENTS

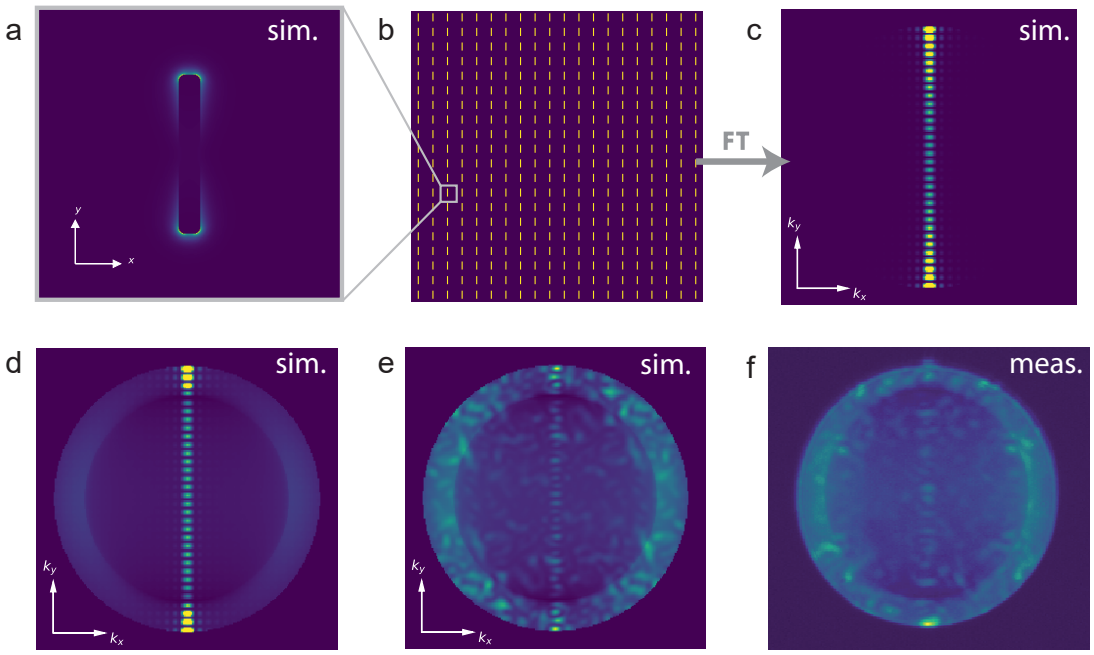

Fig. S 6. Noise study of the bare gold array. (a) Simulated electric field intensity distribution of the rod plasmonic resonance. (b) Illustration of the spatial arrangement of rods forming a 20 x 20 array. (c) Calculation of k-space of the 2D array assembly by a two-dimensional Fourier transformation. (d) Resulting k-space for a Gaussian excitation for dipoles on a glass substrate, supplemented by incoherent background (origin explained in the main text). (e) Final k-space calculation by employing random spatial fluctuations of the amplitude of individual rods (f) Measured SHG emission k-space of a bare gold array system.

Noise features in the background of the measurements (Figure 3b) motivated a numerical study of the SHG emission pattern of a bare gold array. The SHG emission measured at the back focal plane is shown in Figure S6f. For resonant excitation the emission is suppressed as described in the main text.

In order to assemble a model we look at the resonance intensity distribution for a single rod as shown in Figure S6a. The absolute value of the SHG electric field on the rod surface is assumed to have a similar distribution to the intensity of the excited resonant field due to the square relation between the two fields. In order to form complex fields for the calculation we assume a difference of phase π between the two rod ends. Hence, an array of complex fields can be assembled as illustrated in Figure S6b. The k-space of the array SHG emission is then calculated with a two-dimensional Fourier transformation (FT). Figure S6c shows the absolute value of the field calculated in k-space. To further match the conditions of the measurement to the simulation we take into account the Gaussian spatial distribution of the excitation beam. Moreover, we multiply the resulting complex k-space with the corresponding far-field emission of a dipole on a glass substrate. Finally, we add incoherent background in a ratio with the coherent emission estimated by spectral measurements (Figure S2a). These modifications lead to the resulting k-space shown in Figure S6d. The ring in high $|k_{x,y}|$ values is formed due to the air-glass interface that favors emission in higher angles.

Finally, real-space measurements have shown that the emission is fluctuating between rods due to geometrical imperfections. By statistically evaluating this fluctuation we calculated an expected 20% deviation around a mean value. Embedding this random spatial fluctuation in the simulation in form of a normal statistical distribution we receive the k-space of the model accommodating the noise that we observe in the measurements as shown in Figure S6e. These results lead us to conclude that the residual emission of the bare gold array measured is a product of the aforementioned noise sources.